



**HAL**  
open science

# Dynamic-mode-decomposition of the wake of the NREL-5MW wind turbine impinged by a laminar inflow

Giovanni de Cillis, Onofrio Semeraro, Stefano Leonardi, Pietro de Palma,  
Stefania Cherubini

## ► To cite this version:

Giovanni de Cillis, Onofrio Semeraro, Stefano Leonardi, Pietro de Palma, Stefania Cherubini. Dynamic-mode-decomposition of the wake of the NREL-5MW wind turbine impinged by a laminar inflow. *Renewable Energy*, 2022, 199, pp.1-10. 10.1016/j.renene.2022.08.113 . hal-03854591

**HAL Id: hal-03854591**

**<https://hal.science/hal-03854591v1>**

Submitted on 15 Nov 2022

**HAL** is a multi-disciplinary open access archive for the deposit and dissemination of scientific research documents, whether they are published or not. The documents may come from teaching and research institutions in France or abroad, or from public or private research centers.

L'archive ouverte pluridisciplinaire **HAL**, est destinée au dépôt et à la diffusion de documents scientifiques de niveau recherche, publiés ou non, émanant des établissements d'enseignement et de recherche français ou étrangers, des laboratoires publics ou privés.

# Dynamic-mode-decomposition of the wake of the NREL-5MW wind turbine impinged by a laminar inflow

Giovanni De Cillis<sup>1</sup>, Onofrio Semeraro<sup>3</sup>, Stefano Leonardi<sup>2</sup>, Pietro De Palma<sup>1</sup>, Stefania Cherubini<sup>1,\*</sup>

---

## Abstract

Dynamic mode decomposition (DMD) has been applied to the wake of the NREL-5MW wind turbine impinged by a uniform inflow, to identify the most dynamically relevant coherent structures characterizing this flow. The decomposition has been applied on a snapshot dataset obtained by Large-Eddy Simulation of the flow impinging on the wind turbine, whose tower and nacelle are modeled by the immersed boundary method, whereas rotor blades are modeled using the actuator line method. The Sparsity-Promoting DMD algorithm allows one to select a limited number of dynamic modes optimally reconstructing the snapshot sequence. Among the largest-amplitude selected modes, we found the tip vortices, oscillating at an angular frequency equal to three times the rotational frequency of the turbine. Interestingly, the remaining selected modes are characterized by low frequencies and large-scale spatial structures, reaching the frequency range of the wake meandering. This small set of dynamic modes is highly relevant for the formulation of accurate reduced-order models, which would eventually lead to the design of optimized wind farms layout and control to increase the energy density produced.

*Keywords:* Dynamic Mode Decomposition, NREL-5MW wind turbine, Turbine wake, coherent structures, Reduced-order-models, Modal decomposition

---

## 1. INTRODUCTION

An accurate description and modeling of the complex behaviour of fluid flows relevant to many energy-related applications still poses a great challenge to researchers and engineers, especially in view of the upcoming energy transition [1]. Notable examples are the flows in a combustion chamber [2] and the flow impinging on a wind turbine [3], both exhibiting non trivial and coherent oscillations that markedly affect the energy production. In this work we focus on wind turbines, whose production is likely to become crucial in the upcoming years [4].

For limiting the impact of energy production by fossil fuels on the environment, an increasingly larger fraction of energy demand should be satisfied by renewable sources [5], such as wind turbines. In particular, it is expected that wind power would be able to provide about 35% of the total electricity needs by 2050 [6], reaching 6000 *GW* of power production. However, in the last few years, the wind-energy electricity capacity have reached only  $\approx 9\%$ , corresponding to about 700 *GW* [7]. In order to meet the Paris goal, an average power addition of 180 *GW* per year would be needed.

The cost of electricity generated from onshore wind is decreasing, with the global average falling to USD 53/*MWh* in 2019 [8]. The levelised cost of electricity (LCOE) for onshore wind plants is now competitive with respect to fossil fuel generation sources and is expected to decrease further as installation costs reduce and performance improve. Instead, the LCOE

---

\*stefania.cherubini@polib.it

<sup>1</sup>Dipartimento di Meccanica, Matematica e Management, Politecnico di Bari, Via Re David 200, Bari, Italy

<sup>2</sup>Department of Mechanical Engineering, University of Texas, Dallas, Texas, USA

<sup>3</sup>LISN, Université de Paris-Saclay, CNRS, Orsay, France

26 of offshore wind plants is competitive in certain European markets (such as Germany and the  
27 Netherlands) and would most probably become competitive in other markets by 2030, dropping  
28 from the actual average of  $120 \text{ USD}/\text{MWh}$  in 2019 to an average of  $30 - 70 \text{ USD}/\text{MWh}$  by  
29 2050 [6, 9].

30 Despite this encouraging drop of the costs, the current rate of growth of wind-energy installed  
31 power is still too low for reaching the Paris climate goals [8]. The needed acceleration in the  
32 deployment of wind power installations will require the enhancement of policy support initia-  
33 tives, eradication of regulatory uncertainties, and still more investment in new technologies [8].  
34 In particular, technology innovation is needed for both the single turbine and the farm arrange-  
35 ment.

36 Thanks to the increase of rotor diameters and hub heights, a considerable rise in the capacity  
37 of the single turbine would be reached by 2035 (namely,  $5 - 6 \text{ MW}$  for onshore applications,  
38 and  $15 - 20 \text{ MW}$  for offshore ones, more than doubling the current capacity of these turbines  
39 [10]). However, wind turbines are usually clustered in large farms, where most of the turbines  
40 operate in the wake of upwind ones. This turbines are rarely capable to achieve the nominal  
41 power production, being exposed to velocity deficit and high turbulence levels [11]. An opti-  
42 mization of the farm design, allowing to fruitfully exploit the interaction of the wakes with the  
43 downwind turbines, would be needed to guarantee high efficiency, flexibility and security of  
44 the power generation, leading us to the topic of the present work.

45 In order to investigate in detail the effect on power production of the interaction of two turbine's  
46 wakes, one should numerically simulate the whole flow field ranging from a few diameters pre-  
47 ceding the upwind turbine to several diameters downstream the second turbine. This task being  
48 computationally prohibitive, the development of low-dimensional models of the wake dynam-  
49 ics that can be fed into simulations of the downwind turbines are going to assume a huge  
50 scientific interest. In fact, the development of such low-dimensional models would allow to  
51 accurately estimate the power production of these turbines at a much cheaper computational  
52 cost. As a consequence, it would be eventually possible to consistently increase the power  
53 produced by the whole wind farm, by simply optimizing the relative placement of the turbines.  
54 Thus, constructing low-dimensional models of the dynamics of wind turbine wakes appears  
55 fundamental for the design and optimization of wind farms. This motivates the present work,  
56 which provides a detailed study of the dynamics of the wake of the  $5 \text{ MW}$  wind turbine aiming  
57 at extracting the dynamically relevant structures, that can be used to develop advanced low-  
58 dimensional models of the wake.

59 In the last years, several attempts have been made to study the dynamics of the wind-turbine  
60 wake by using the Proper Orthogonal Decomposition (POD) method [12] for the formulation  
61 of Reduced-Order Models. This modal decomposition, based on orthogonal modes, has been  
62 applied: for developing low-order models [13]; to array of turbines in order to study the effect  
63 of the layout of the farm [14]; to a single turbine including a detailed description of the effects  
64 of the tower and the nacelle [15].

65 However, recent works [16] have demonstrated that POD suffers from two main drawbacks.  
66 The first is that this method recovers the most energetic structures within the flow, but the en-  
67 ergy may not in all circumstances be the correct measure to rank the flow structures. Moreover,  
68 since second-order statistics are chosen as a basis for the decomposition, valuable phase in-  
69 formation is lost. Thus, the most-energetic POD modes are not always dynamically relevant,  
70 therefore the selection of a low-dimensional basis for the realization of a reduced-order model  
71 may be not trivial [17].

72 For these reasons, we provide in the present work an analysis based on a different recently-  
73 developed approach known as the Dynamic Mode Decomposition (DMD) [16]. This tech-  
74 nique, which allows one to approximate the nonlinear dynamics embedded in a data sequence,  
75 has been recently applied to several complex flow cases, from the flow over a wall-mounted  
76 roughness element [18], to the instabilities developing in several types of combustors [19].  
77 Very recently, the same technique has been successfully used for reconstructing coherent struc-  
78 tures developing on turbomachinery applications such as the gas-liquid flow in a rotodynamic  
79 multiphase pump [20, 21] and the tip leakage vortex in a mixed flow pump [22].  
80 At the moment, very few studies have applied DMD on wind turbine flows. Iungo et al. [23]  
81 focused on the development of reduced models of the wake. Le Clainche et al. [24] applied  
82 DMD to a lidar database for wind predictions. Debnath et al. [25] employed the DMD for  
83 predicting the dynamics of coherent vorticity structures of wind turbine wakes. However, in  
84 most of these works, the DMD modes are ranked with respect to their amplitude, which can  
85 be an ineffective criterion for selecting a very limited subset of dynamic modes, leading to an  
86 unsatisfying quality of the resulting approximation of numerically generated snapshots through  
87 low-order reduced models.  
88 For this reason, in this work we use the Sparsity-Promoting variant of the DMD [26] for rank-  
89 ing the most relevant DMD modes of the three-dimensional numerical dataset. Based on this  
90 robust ranking, a detailed analysis of the main spatial structures and frequencies of the dy-  
91 namically relevant motion in a wind turbine wake, including the tower and the nacelle, is  
92 carried out. Moreover, the convergence of the main frequencies and growth rates, with re-  
93 spect to the low-dimensional basis on which this decomposition is constructed, is assessed for  
94 high Reynolds-number wind-turbine flows. Large Eddy Simulations using the Actuator Line  
95 Method to simulate the rotor and the Immersed Boundary Method to simulate tower and nacelle  
96 are employed to construct the database on which DMD is performed. The Sparsity-Promoting  
97 variant of the DMD algorithm is then applied for identifying and analysing the most relevant  
98 coherent structures embedded in the turbulent wake flow.

## 99 2. LARGE EDDY SIMULATION

Large Eddy Simulations (LES) is employed for studying the wake behind the NREL-5MW  
wind turbine. LES resolves large-scale turbulent structures, filtering out small-scale turbulent  
fluctuations, whose effect on the large flow structures is modelled [27]. This is done by solving  
the governing equations for the filtered non-dimensional velocity,  $\mathbf{u}$ , derived from the incom-  
pressible Navier–Stokes equations:

$$\frac{\partial u_i}{\partial t} + \frac{\partial u_i u_j}{\partial x_j} = -\frac{\partial p}{\partial x_i} + \frac{1}{Re} \frac{\partial^2 u_i}{\partial x_j \partial x_j} - \frac{\partial \tau_{ij}}{\partial x_j} + F_i, \quad (1)$$

$$\frac{\partial u_i}{\partial x_i} = 0, \quad (2)$$

100 where  $i, j \in \{1, 2, 3\}$  indicate the components corresponding to the streamwise,  $x$ , wall-  
101 normal,  $y$ , and spanwise,  $z$ , directions, respectively, and  $p$  denotes the pressure. The Reynolds  
102 number is defined as  $Re = \frac{U_\infty D}{\nu}$ , where  $U_\infty$  is the inlet velocity,  $D$  is the rotor diameter and  $\nu$   
103 is the kinematic viscosity of the fluid. These quantities have been used as reference variables  
104 for non-dimensionalisation.

105 The residual stress tensor,  $\tau_{ij}$ , is decomposed into an isotropic and an anisotropic part. The

106 isotropic part is included in the modified filtered pressure  $p^* = p + \frac{1}{3}\tau_{ii}$ , whereas the anisotropic  
 107 part needs to be modelled. As in many previous works [28, 15], the Smagorinsky model is em-  
 108 ployed, which relates the residual stress to the filtered rate of strain by means of the eddy  
 109 viscosity of the residual motion,  $\nu_r$ , which is modelled using the mixing length hypothesis,  
 110 with Smagorinsky constant  $C_S$  set to 0.17.

111 The term  $F_i$  in equation (1) models the aerodynamic force (per unit length) exerted by the tur-  
 112 bine blades on the fluid, as provided by the actuator line method, [29]. Whereas, the immersed  
 113 boundary method [30], based on a discrete forcing approach is used for describing the tower  
 114 and nacelle.

115 The governing equations are solved by means of an in-house numerical code, written in For-  
 116 tran90. This code implements a second-order-accurate centered finite difference scheme for the  
 117 spatial discretization, on a staggered Cartesian grid. A hybrid low-storage third-order-accurate  
 118 Runge-Kutta scheme is used for time integration. [31]. Further details on the numerical ap-  
 119 proach can be found in [32, 15].

120 For the considered NREL-5MW wind turbine, the Reynolds number based on the turbine di-  
 121 ameter and the inlet velocity at hub-height is  $Re = 10^8$ . The tip-speed ratio considered in this  
 122 study is  $\lambda = 7$ . The computational domain has extension  $12.5D \times 5D \times 3D$  in the streamwise,  
 123 vertical and transverse directions, respectively. The turbine is located at  $4D$  from the inlet,  
 124 centered in the transverse direction. Concerning the wall-normal direction, we set  $y = 0$  on the  
 125 nacelle's center, the wall being placed at  $y = -0.9$ .

126 This computational domain is discretized in space using  $2048 \times 512 \times 512$  grid-points in  $x$ ,  $y$   
 127 and  $z$  directions, respectively. The grid is uniform along the streamwise and transverse direc-  
 128 tions, and is stretched in the vertical direction, with finer grid spacing in the turbine's wake. In  
 129 particular, of the total 512 points used in the wall-normal direction, 250 points are uniformly  
 130 gathered in the region going from  $y = -0.9$  to  $y = 0.6$ , which comprises the rotor's and the  
 131 tower's wakes. The remaining 262 points are distributed in the region  $y \in [0.6, 5]$ , stretched  
 132 towards the upper boundary following an hyperbolic tangent law.

133 At the domain boundaries, we imposed the following conditions: at the outlet points, a radia-  
 134 tive non-reflective boundary condition with convection velocity  $C = 9 \text{ m/s}$  [33]; no-slip at the  
 135 bottom wall; free slip at the top wall; periodicity along the spanwise direction.

136 Concerning time integration, in order to guarantee a uniform time spacing of the snapshots for  
 137 the DMD analysis (see the next subsection), we set a fixed time step  $dt = 0.00073$ , ensuring a  
 138 Courant-Friedrichs-Lewy number  $< 0.5$  throughout the whole computation.

### 139 3. SPARSITY PROMOTING DYNAMIC MODE DECOMPOSITION

The dynamic mode decomposition (DMD), introduced in [16], is a data driven technique which  
 allows one to extract relevant flow features, namely the DMD modes, whose dynamics is gov-  
 erned by corresponding eigenvalues. The variant we employ in the present study has been  
 developed in [26] and is called Sparsity Promoting Dynamic Mode Decomposition (SP-DMD),  
 since it selects a limited number of modes which optimally reconstruct the flow field time se-  
 ries.

A series of  $M$  snapshots is collected from the LES at a constant sampling frequency. Each  
 snapshot  $\mathbf{q}^i$  can include one or multiple flow variables or even derived observables and has  
 dimension  $N = O \times S$  ( $\mathbf{q}^i \in \mathbb{C}^N$ ), where  $O$  is the number of observables considered, whereas

$S$  represents the number of measurements points:

$$\{\mathbf{q}^1, \mathbf{q}^2, \dots, \mathbf{q}^M\}. \quad (3)$$

We assume that a linear time-invariant mapping  $\mathbf{A}$ , connects every pair of successive snapshots,

$$\mathbf{q}^{i+1} = \mathbf{A}\mathbf{q}^i, \quad i = \{0, \dots, M-1\}. \quad (4)$$

Using relation (4) we can write:

$$\mathbf{Q}^1 = \mathbf{A}\mathbf{Q}^0, \quad (5)$$

where  $\mathbf{Q}^0$  and  $\mathbf{Q}^1$  are:

$$\mathbf{Q}^0 = [\mathbf{q}^0 \ \mathbf{q}^1 \ \dots \ \mathbf{q}^{M-1}], \quad (6)$$

$$\mathbf{Q}^1 = [\mathbf{q}^1 \ \mathbf{q}^2 \ \dots \ \mathbf{q}^M]. \quad (7)$$

The linear operator  $\mathbf{A}$ , as suggested by [16], can be projected onto the  $r$ -dimensional POD basis  $\mathbf{U}$  of the snapshots matrix  $\mathbf{Q}^0$ , calculated using a Singular Value Decomposition (SVD) or the snapshot method [34],

$$\mathbf{Q}^0 = \mathbf{U}\mathbf{S}\mathbf{V}^*, \quad (8)$$

$$\mathbf{A} \approx \mathbf{U}\mathbf{F}\mathbf{U}^*. \quad (9)$$

The matrix  $\mathbf{F}$  can be therefore obtained by minimizing the Frobenius norm of the difference between  $\mathbf{Q}^1$  and  $\mathbf{A}\mathbf{Q}^0$ , with  $\mathbf{A} = \mathbf{U}\mathbf{F}\mathbf{U}^*$  and  $\mathbf{Q}^0 = \mathbf{U}\mathbf{S}\mathbf{V}^*$ ,

$$\min_{\mathbf{F}} \|\mathbf{Q}^1 - \mathbf{U}\mathbf{F}\mathbf{S}\mathbf{V}^*\|_F^2. \quad (10)$$

The optimal solution to (10) is:

$$\mathbf{F} = \mathbf{U}^*\mathbf{Q}^1\mathbf{V}\mathbf{S}^{-1}. \quad (11)$$

This projection ensures a more robust calculation of the low dimensional representation of  $\mathbf{A}$  and it allows also to account for a rank-deficiency of the snapshots matrix  $\mathbf{Q}^0$ , restricting the basis  $\mathbf{U}$  to those vectors associated to non-zero singular values, or singular values above a prescribed threshold. The dynamics in the low-dimensional subspace defined by the POD modes  $\mathbf{U}$  is governed by

$$\mathbf{x}^{i+1} = \mathbf{F}\mathbf{x}^i. \quad (12)$$

Dynamic modes are then extracted by computing the eigendecomposition of the matrix  $\mathbf{F}$ :

$$\mathbf{F} = \underbrace{[\mathbf{y}_1 \ \dots \ \mathbf{y}_r]}_{\mathbf{Y}} \underbrace{\begin{bmatrix} \mu_1 & & \\ & \ddots & \\ & & \mu_r \end{bmatrix}}_{\mathbf{D}_\mu} \underbrace{\begin{bmatrix} \mathbf{z}_1^* \\ \vdots \\ \mathbf{z}_r^* \end{bmatrix}}_{\mathbf{Z}^*} \quad (13)$$

where  $\mathbf{y}_i$  and  $\mathbf{z}_i^*$  are the right and left eigenvectors of  $\mathbf{F}$ , which are scaled such that  $\mathbf{y}_i^*\mathbf{y}_i = 1$  and  $\mathbf{z}_i^*\mathbf{y}_j = \delta_{ij}$ . Therefore the solution to (12) can be calculated as follows:

$$\mathbf{x}^n = \mathbf{Y}\mathbf{D}_\mu^n\mathbf{Z}^*\mathbf{x}^0 = \sum_i^r \mathbf{y}_i\mu_i^n\mathbf{z}_i^*\mathbf{x}^0 = \sum_i^r \mathbf{y}_i\mu_i^n\alpha_i, \quad (14)$$

where  $\alpha_i = \mathbf{z}_i^* \mathbf{x}^0$  represents the component of the initial condition  $\mathbf{x}^0$  in the  $\mathbf{z}_i^*$  direction. The snapshots can be approximated by mapping  $\mathbf{x}^i$  on the higher dimensional space  $\mathbb{C}^N$ ,

$$\mathbf{q}^n \approx \mathbf{U} \mathbf{x}^n = \sum_i^r \mathbf{U} \mathbf{y}_i \mu_i^n \alpha_i = \sum_i^r \phi_i \mu_i^n \alpha_i, \quad (15)$$

and can be seen, therefore, as a linear combination of the DMD modes  $\phi_i = \mathbf{U} \mathbf{y}_i$  where  $\alpha_i$  is the amplitude of the corresponding DMD mode. The equation (15) can be written also in matrix form:

$$\underbrace{[\mathbf{q}^0 \quad \mathbf{q}^1 \quad \dots \quad \mathbf{q}^{M-1}]}_{\mathbf{Q}^0} \approx \underbrace{[\phi_1 \quad \phi_2 \quad \dots \quad \phi_r]}_{\Phi} \underbrace{\begin{bmatrix} \alpha_1 & & & \\ & \alpha_2 & & \\ & & \ddots & \\ & & & \alpha_r \end{bmatrix}}_{D_\alpha} \underbrace{\begin{bmatrix} 1 & \mu_1 & \dots & \mu_1^{M-1} \\ 1 & \mu_2 & \dots & \mu_2^{M-1} \\ \vdots & \vdots & \ddots & \vdots \\ 1 & \mu_r & \dots & \mu_r^{M-1} \end{bmatrix}}_{V_{and}}, \quad (16)$$

which highlights that the temporal evolution of the dynamic modes is governed by the Vandermonde matrix  $V_{and}$ . Once the eigendecomposition of (13) is computed, the calculation of the amplitudes vector  $\alpha = [\alpha_1 \dots \alpha_r]^T$  is performed solving the following optimization problem.

$$\min_{\alpha} J(\alpha) = \|\mathbf{Q}^0 - \Phi D_\alpha V_{and}\|_F^2. \quad (17)$$

The latter, using equation (8) and the relation and the definition of the matrix  $\Phi := \mathbf{U} \mathbf{Y}$ , can be rewritten as:

$$\min_{\alpha} J(\alpha) = \|\mathbf{S} \mathbf{V}^* - \mathbf{Y} D_\alpha V_{and}\|_F^2. \quad (18)$$

The superposition of all the DMD modes, weighted by their amplitudes and evolving according to their frequency and growth rate, optimally approximates the data sequence. However, the sparsity promoting DMD aims at finding a low dimensional representation of the snapshots' sequence in order to capture the most relevant dynamic structures.

This objective is achieved in two steps: firstly, a sparsity structure is sought, which achieves a user-defined trade-off between the number of modes and the approximation error; then the sparsity structure of the amplitudes' vector is fixed and the optimal values of the non-zero amplitudes is calculated. The first step is tackled by augmenting the objective function  $J(\alpha)$  in (18) with an additional term,  $\mathbf{card}(\alpha)$ , the penalizes the number of non-zero elements in the amplitudes' vector  $\alpha$ ,

$$\min_{\alpha} J(\alpha) + \gamma \mathbf{card}(\alpha). \quad (19)$$

In the sparsity promoting optimization problem (19),  $\gamma$  is a parameter that influences the sparsity level, with higher values of the parameter promoting sparser solutions. In general, finding a solution to (19) amounts to a combinatorial search that quickly becomes intractable for any problem of interest. For this reason a relaxed version of (19) is introduced by replacing the cardinality function of  $\alpha$  with its  $\ell_1$ -norm,

$$\min_{\alpha} J(\alpha) + \gamma \sum_{i=1}^r |\alpha_i|. \quad (20)$$

The sparsity-promoting DMD problem (20) is a convex optimization problem, solved using the ADMM [26]. Then, the sparsity structure of the amplitudes' vector is fixed and the amplitudes of the non-zero entries are recomputed by solving the following optimization problem:

$$\begin{aligned} & \underset{\alpha}{\text{minimize}} && J(\alpha) \\ & \text{subject to} && E^T \alpha = 0, \end{aligned} \quad (21)$$

where the matrix  $E \in \mathbb{R}^{r \times m}$  encodes the sparsity structure of the amplitudes' vector  $\alpha$ . The columns of  $E$  are unitary vectors whose non-zero elements correspond to zero components of  $\alpha$ . For example, for  $\alpha \in \mathbb{C}^4$  with:

$$\alpha = [\alpha_1 \quad 0 \quad \alpha_3 \quad 0]^T \quad (22)$$

the matrix  $E$  will be:

$$E = \begin{bmatrix} 0 & 0 \\ 1 & 0 \\ 0 & 0 \\ 0 & 1 \end{bmatrix}. \quad (23)$$

140 The numerical method employed for the solution of the optimization problem (21) is the one  
141 proposed in [26].

## 142 4. RESULTS

143

144 In order to carrying out the DMD analysis, we extract from the snapshots of the velocity  
145 field a reduced three-dimensional subdomain enclosing the wake. As shown in the sketch in  
146 figure 1, the considered subdomain begins at  $x = 0$ ,  $y = -0.7$ ,  $z = -0.7$  and extends towards  
147  $x = 8.4$ ,  $y = 0.63$ ,  $z = 0.7$  in the  $x$ ,  $y$  and  $z$  directions, respectively. Notice that, since the  
148 computational domain is centered at the nacelle location in the spanwise direction, the selected  
149 subdomain comprises the whole region of the wake, starting just downstream of the rotor and  
150 extending towards the outlet, while in the wall-normal direction it extends from the wall up  
151 to the upmost position reached by the tip of the blades. Figure 2 provides a snapshot of the  
152 flow field in such a subdomain showing, by means of the  $\lambda_2$  criterion [35], the coherent set of  
153 tip- and root-vortices generated by the rotor's blades. These vortices remain rather coherent up  
154 to  $\approx 3 - 4$  diameters downstream of the turbine, and then break down to turbulence further  
155 downstream. However, some coherent vortex filaments can be observed in the downstream  
156 part of the domain, indicating that the dynamics of the wake is not only driven by incoherent  
157 fluctuations.

158 The whole flow field in the selected subdomain is stored at time intervals  $\Delta t$  corresponding to  
159 a  $10^\circ$  rotation of rotor. The entire dataset comprises 3052 snapshots, whose ensemble average  
160 is shown in Figure 3. One can observe that the wake is asymmetric and that smaller wakes are  
161 present right behind the tower and at the center of the wake, as shown in the bottom right frame  
162 of figure 3. Notice that the snapshots' ensemble average is subtracted from each snapshot be-  
163 fore applying the DMD, which makes all the eigenvalues lie on the unitary circle[36]. Small  
164 deviations from this theoretical condition will be observed because we perform the decompo-  
165 sition in reduced POD subspaces.

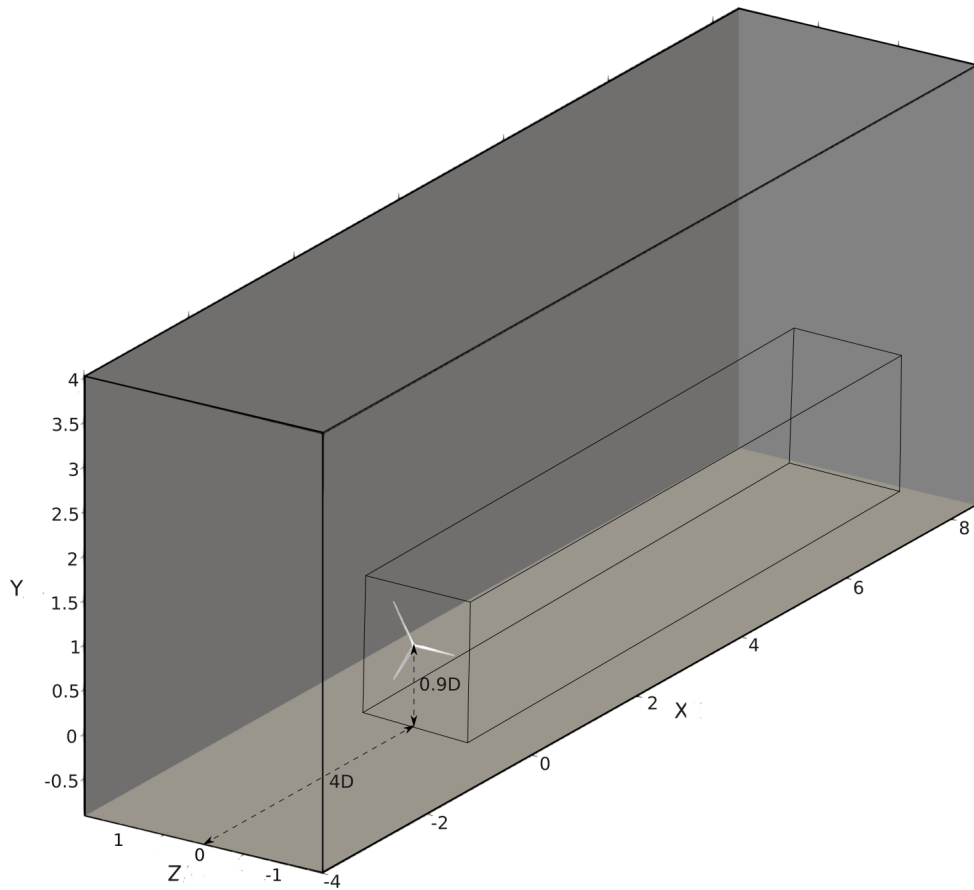


Figure 1: Sketch of the computational setting indicating the subdomain selected for the DMD analysis.

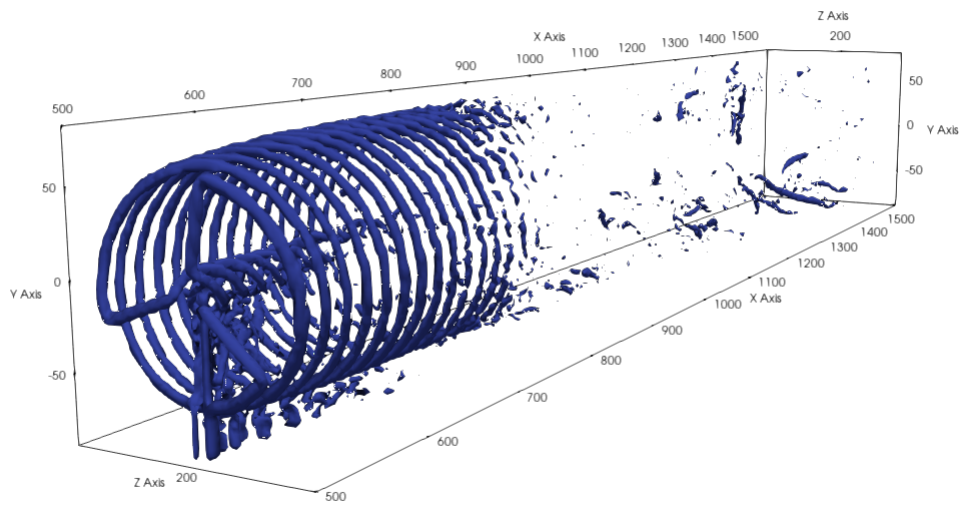


Figure 2: Snapshot of the flow field showing the  $\lambda_2$  criterion. The axis labels refer to the grid points, in order to specify the mesh points distribution.

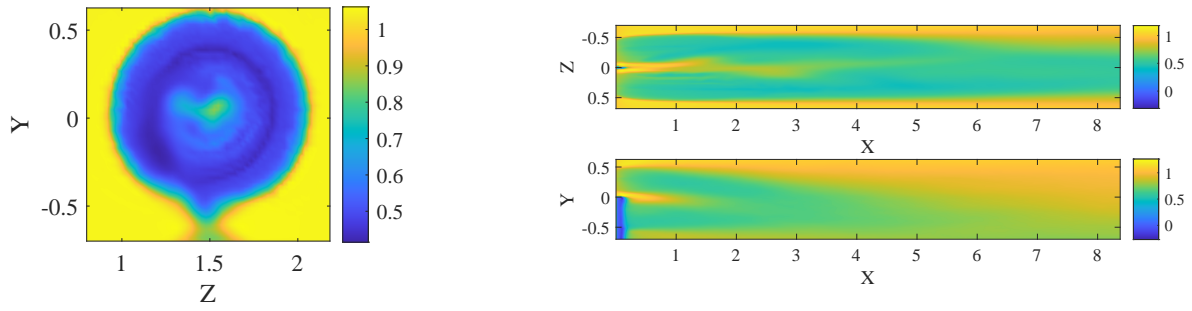


Figure 3: Ensemble average of the LES snapshots: streamwise velocity in the plane  $x = 3$  (left),  $y = 0$  (top right), and  $z = 0$  (bottom right).

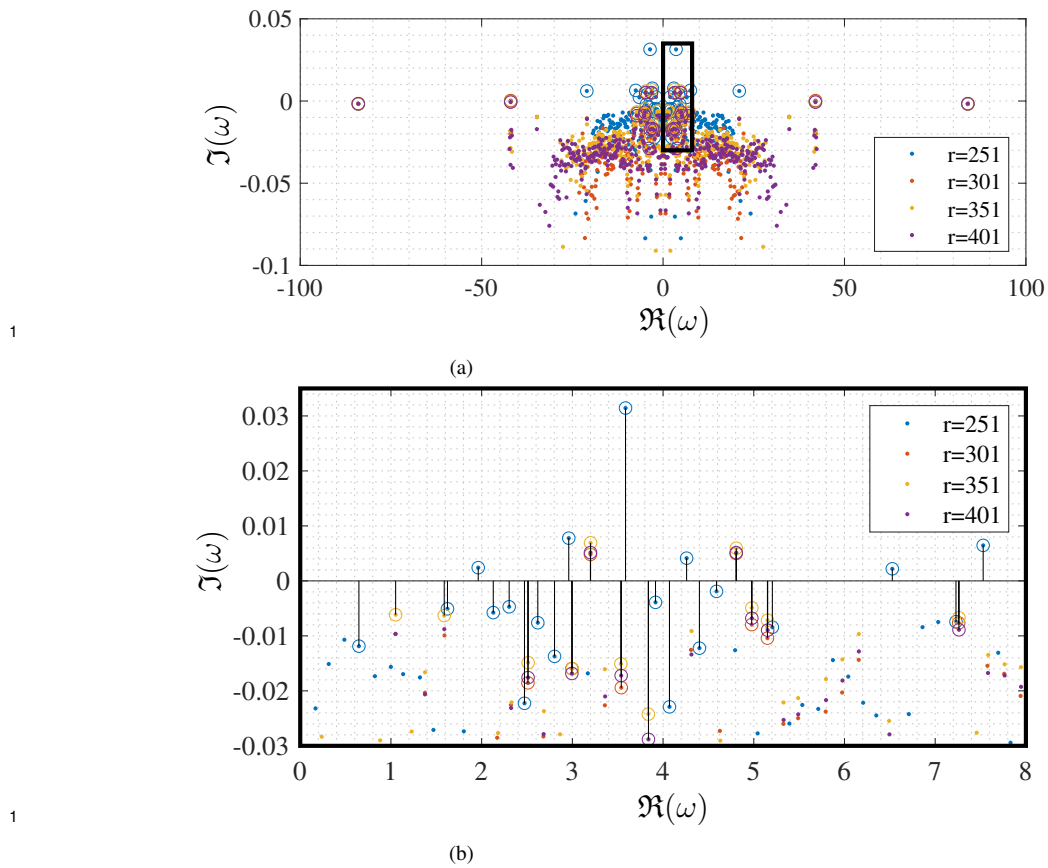


Figure 4: Convergence of the DMD spectrum with respect to the dimension  $r$  of the POD basis: (a) entire spectrum and (b) close-up. Circled dots correspond to the selected modes for each  $r$  with  $\gamma = 29181$ .

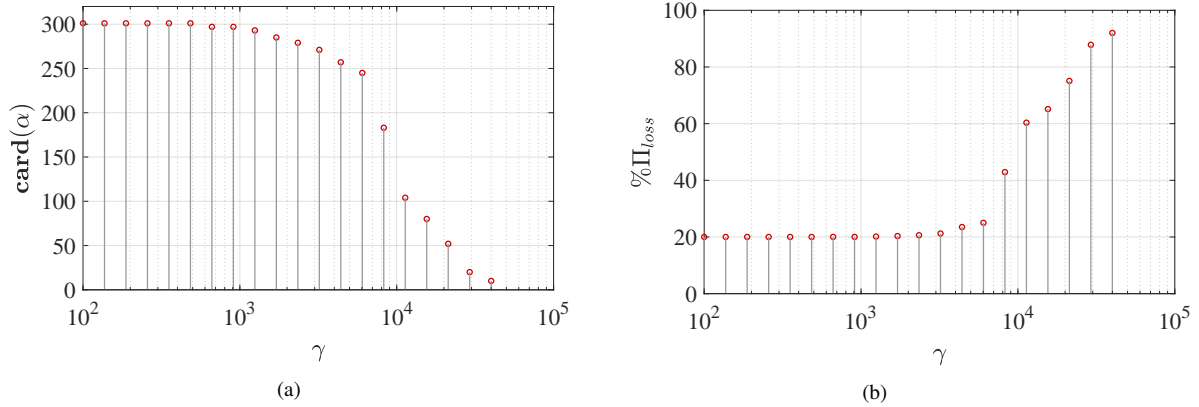


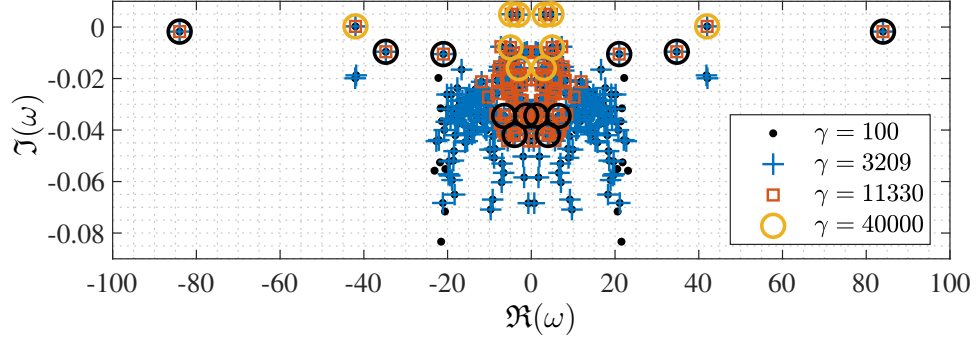
Figure 5: The sparsity level  $\text{card}(\alpha)$  (a) and the optimal performance loss  $\% \Pi_{\text{loss}}$  (b) for different values of the sparsity parameter  $\gamma$ .

166 In order to ensure the convergence of the dynamical modes with respect to the dimension of  
 167 the chosen POD basis, the sparsity promoting DMD has been carried out for different values  
 168 of the POD subspace dimension,  $r$ . Figure 4 shows the logarithmic mapping of the eigenvalues  
 169 for different values of  $r$ , computed according to  $\omega = -\frac{\log(\mu)}{i\Delta t}$ , where  $\Delta t$  is the time interval  
 170 between two consecutive snapshots and  $i$  the imaginary unit. Notice that the eigenvalues (as  
 171 well as the associated dynamic modes) form complex conjugate pairs, since the decomposed  
 172 velocity field is constituted of real variables.

173 Concerning the influence of the POD subspace dimension on the DMD spectrum, one can ob-  
 174 serve in the top panel of figure 4, that increasing this parameter, for sufficiently high value of  $r$   
 175 the spectra collapse onto each other. In particular, the bottom panel of figure 4 shows that for  
 176  $r \geq 301$ , the eigenvalues' frequencies are very well converged, and only small deviations are  
 177 recovered on the associated growth rates of the modes. However, as expected for a turbulent  
 178 statistically-stationary flow, the eigenvalues should collapse onto the unit circle (corresponding  
 179 to a zero growth rate), due to the quasi periodic dynamics of the associated modes. Thus, this  
 180 small deviation of the growth rate is a consequence of the numerical approximation and has  
 181 no physical meaning. The behavior shown in the bottom frame of figure 4 indicates that fur-  
 182 ther increasing the subspace dimension would not provide any improvement in the numerical  
 183 estimate of the growth rate. For this reason, the following analyses have been carried out with  
 184  $r = 301$ , which is to be considered satisfactory.

185 The influence of the sparsity parameter  $\gamma$  on the DMD modes is now assessed, by repeating  
 186 the computation for different values of  $\gamma$ , ranging from 100 to 40000, quasi equally spaced in  
 187 logarithmic scale. As shown in Figure 5, low (high) values of  $\gamma$  ensure the selection of a large  
 188 (small) number of DMD modes. Notice that, even for very low values of  $\gamma$ , the performance  
 189 loss is not null since the DMD is carried out on a lower-dimensional POD projection of the  
 190 snapshot's space.

191 For the considered case, when  $\gamma < 8 \times 10^3$ , the performance loss with respect to the POD  
 192 basis is negligible. Whereas, for  $\gamma > 8 \times 10^3$ , the performance loss rapidly increases towards  
 193 90%, while the number of selected modes is reduced of more than one order of magnitude. The  
 194 influence of  $\gamma$  on the DMD spectrum is shown in figure 6. With  $\gamma = 40000$ , four pair of modes  
 195 with  $\omega \in (3 - 5)$ , and a larger frequency mode with  $\omega \approx 42$ , are selected. Decreasing the  
 196 sparsity parameter of a factor 4, many other low-frequency modes are selected together with a



1

Figure 6: Eigenvalues of the selected DMD modes for different values of the parameter  $\gamma$ . Black circles correspond to the modes shown in Figure 8.

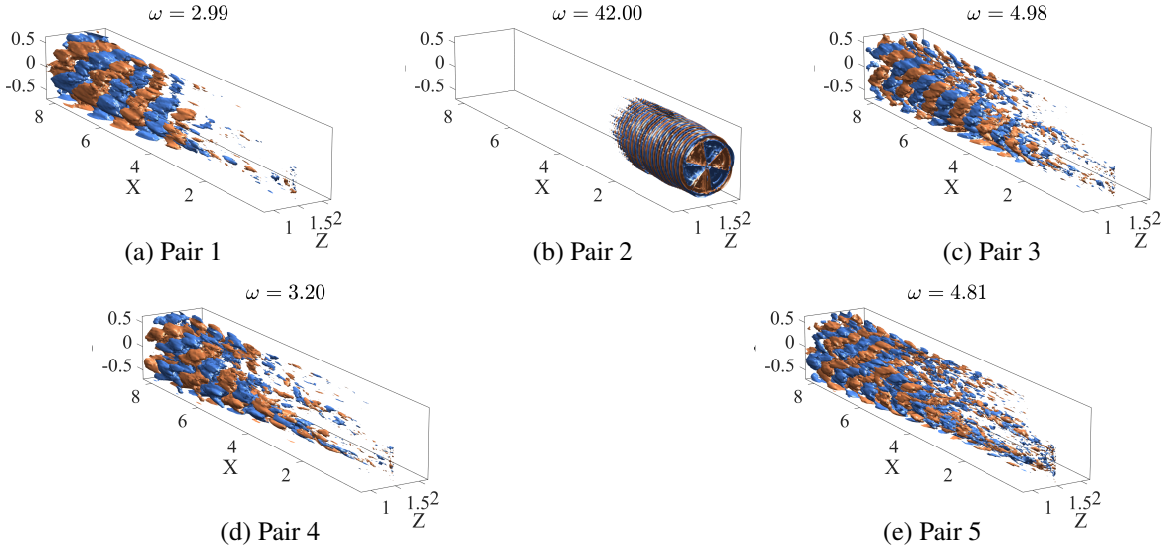


Figure 7: Streamwise velocity iso-surfaces (red for positive, blue for negative values) of the real part of the 5 dynamic modes' pairs selected by the sparsity-promoting algorithm with  $\gamma = 40000$ , ordered according to their amplitude  $|\alpha|$ .

197 few high frequency DMD modes with  $\omega \approx 21$ ,  $\omega \approx 35$ ,  $\omega \approx 84$ . Further decreasing  $\gamma$  to 3209,  
 198 mostly low-frequency modes, in the range  $\omega < 20$ , are added to the spectrum, together with  
 199 two more stable DMD modes with  $\omega = 42$ . Further decreasing the parameter to 100 leads only  
 200 to negligible changes in the spectrum.

201

202 The five pairs of DMD modes selected for  $\gamma = 40000$  are shown in figure 7. The pair corre-  
 203 sponding to  $\omega = 42.00$  is clearly related to the tip vortices (see Figure 7(b)), oscillating at an  
 204 angular frequency equal to three times the rotational frequency of the turbine. The remaining  
 205 selected modes, characterized by rather low frequencies, are associated to large-scale spatial  
 206 structures mostly developing in the far wake region, as can be observed in Figure 7(a,c-e).  
 207 These low-frequency modes are likely to be linked to the secondary instability of the tip vor-  
 208 tices and to their interaction with the vortices shed by the tower, as suggested by the POD  
 209 analysis of the wake of a wind turbine in the presence of tower and nacelle [15].

210 Some of the modes selected for  $\gamma = 11330$  (indicated by the black circles in figure 6), are  
 211 shown in figure 8, ordered according to their amplitude. The largest-amplitude mode shown

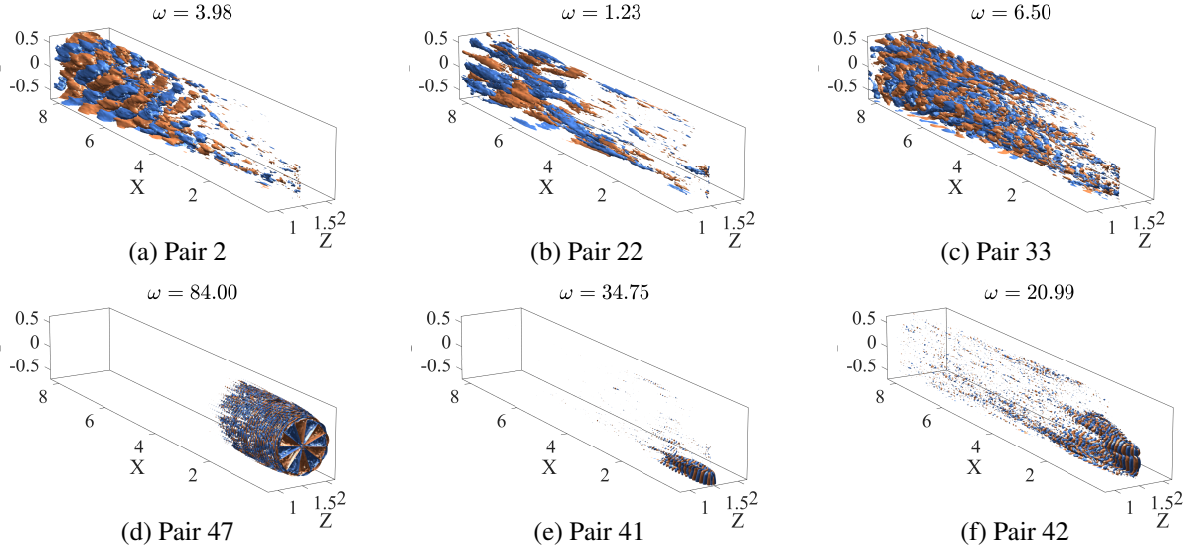


Figure 8: Streamwise velocity iso-surfaces (red for positive, blue for negative values) of the real part of six dynamic modes' pairs selected by the sparsity-promoting algorithm with  $\gamma = 11330$ , ordered according to their amplitude  $|\alpha|$ .

212 in figure 8 (a) are very similar to the low-frequency ones found for  $\gamma = 40000$ . Among the  
 213 largest-amplitude modes, many other DMD modes present a similar spatial structure, associ-  
 214 ated to slightly higher (figure 8 (c)) or lower (figure 8 (b)) spatial and temporal wavenumbers.  
 215 In particular, the mode provided in figure 8 (b) is characterized by a very low frequency corre-  
 216 sponding to a Strouhal number  $St \approx 0.2$  which lies within the frequency range typical of the  
 217 wake meandering [3, 37, 38].

218 High-frequency modes are selected as well for  $\gamma = 11330$ . In particular, among these modes,  
 219 that with the largest amplitude has  $\omega = 84.00$  (see figure 8 (d)), appearing as a harmonic of  
 220 the previously shown DMD mode associated to the tip vortices (see figure 7 (b)). Among the  
 221 lower-amplitude modes, some moderate-frequency modes are present, two of which are shown  
 222 in figure 8 (e-f). These modes appear to be localized in the tower's and nacelle's wake and  
 223 characterized by a fine spatial structures.

224 A two-dimensional visualization of some of these DMD modes is shown in figure 9 (left col-  
 225 umn), together with the Fourier transform in the streamwise direction of their axial velocity  
 226 component averaged on the cross-section (right column). The modes are ordered with increas-  
 227 ing frequency, from top to bottom. The lowest-frequency mode shown in figure 9 (a), whose  
 228 frequency lies in the range of the wake meandering, is characterized by a very low main stream-  
 229 wise wavenumber close to 1.

230 The following three modes, provided in figure 9 (c-e-g) and associated with a Strouhal number  
 231 in the range  $St \approx 0.46 - 0.78$ , are very similar in structure and frequency to the dominant  
 232 modes found by POD in the far wake region of a wind turbine in the presence of tower and  
 233 nacelle [15]. Notice that these frequencies and large-scale oscillations were undetected in a  
 234 modal decomposition of the wake of the wind turbine rotor in the absence of tower and nacelle  
 235 [15], suggesting that the turbine's tower may have a crucial role in the flow dynamics in the  
 236 near and in the far-wake regions.

237 Spatial Fourier transform of these modes allows one to find a dominant streamwise wavenum-  
 238 bers in the range  $\alpha \approx 4 - 5$ , which are consistent with the dominant streamwise wavenumbers

239 recovered by local stability analyses of the wake flow behind low-Reynolds number wind tur-  
240 bines [39, 40]. Notice that, for  $\gamma = 40000$ , four out of the five selected modes are character-  
241 ized by temporal and spatial wavenumbers in this range, suggesting that these large-scale oscilla-  
242 tions have a strong dynamical relevance for the considered flow.

243 As previously discussed, for decreasing values of the sparsity parameter, DMD modes with  
244 finer structures and higher frequencies are found as well. The mode with  $\omega = 6.50$  has a spa-  
245 tial distribution and structure similar to the lower-frequency ones, although characterized by a  
246 larger streamwise wavenumber (figure 9 (i-j)). In particular, being characterized by a dominant  
247  $\alpha \approx 8$ , this mode is likely to represent a harmonic of one of the low-frequency modes shown  
248 in 9 (a-c) which have streamwise wavenumber  $\alpha \approx 4$ .

249 Finally, a two-dimensional visualization of three high-frequency DMD modes is provided in  
250 figure 9 (k-m-o). The first two of these modes are localized in the central region of the domain,  
251 corresponding to the tower’s (and nacelle’s) wake. Unlike the previously discussed modes,  
252 these DMD modes are mostly localized in the near wake and characterized by much higher  
253 streamwise wavenumbers. In particular, one of these two modes has temporal and streamwise  
254 wavenumber equal to half of the tip vortices’ ones (compare figure 9 (k-l) with (o-p)), probably  
255 representing a subharmonic of this high-amplitude DMD mode. Whereas, the other is charac-  
256 terized by a temporal and streamwise wavenumber slightly lower than those of the tip vortices,  
257 with Strouhal number with respect to the tower diameter close to  $\approx 0.22$ . This mode might be  
258 associated to the vortex shedding of the tower. Similar modes were recovered by POD in [15]  
259 for a lower value of the Reynolds number, probably being linked to the interaction of the tip  
260 vortices with the vortices shed by the tower.

## 261 5. CONCLUSIONS

262 The present work provides a numerical study of the dynamically relevant flow motion in  
263 the wake of the NREL-5MW wind turbine. The novelty of this work is in the use of the  
264 Sparsity-Promoting variant of the Dynamic Mode Decomposition (DMD) method based on a  
265 three-dimensional dataset generated by large eddy simulation of the flow through the turbine.  
266 The tower and the nacelle are included in the simulation and are modeled by the immersed  
267 boundary method, whereas rotor blades are modeled using the actuator line method.

268 For dynamically decomposing the wake flow, we extracted flow snapshots in a subdomain  
269 enclosing the wake, stored every  $10^\circ$  rotation of the rotor. The Sparsity-Promoting DMD al-  
270 gorithm has been applied on this data-set, allowing us to select a limited number of dynamic  
271 modes which optimally reconstruct the snapshots’ sequence.

272 This method is applied on a projection of the dataset over a low-dimensional proper-orthogonal-  
273 decomposition (POD) basis. On this low-dimensional basis, the algorithm seeks for a sparsity  
274 structure by minimizing an objective function representing the error with respect to the consid-  
275 ered data-set. The influence of the dimension of the POD subspace on the DMD modes has  
276 been first investigated, showing a good convergence of the DMD spectrum for a POD subspace  
277 dimension  $> 300$ .

278 For high values of the sparsity parameter, only five conjugate pairs of DMD modes are selected.  
279 Among the selected modes, we find one mode corresponding to the tip vortices, oscillating at  
280 an angular frequency equal to three times the rotational frequency of the turbine. The remain-  
281 ing selected modes are all characterized by low frequencies and large-scale spatial structures  
282 developing in the far wake.

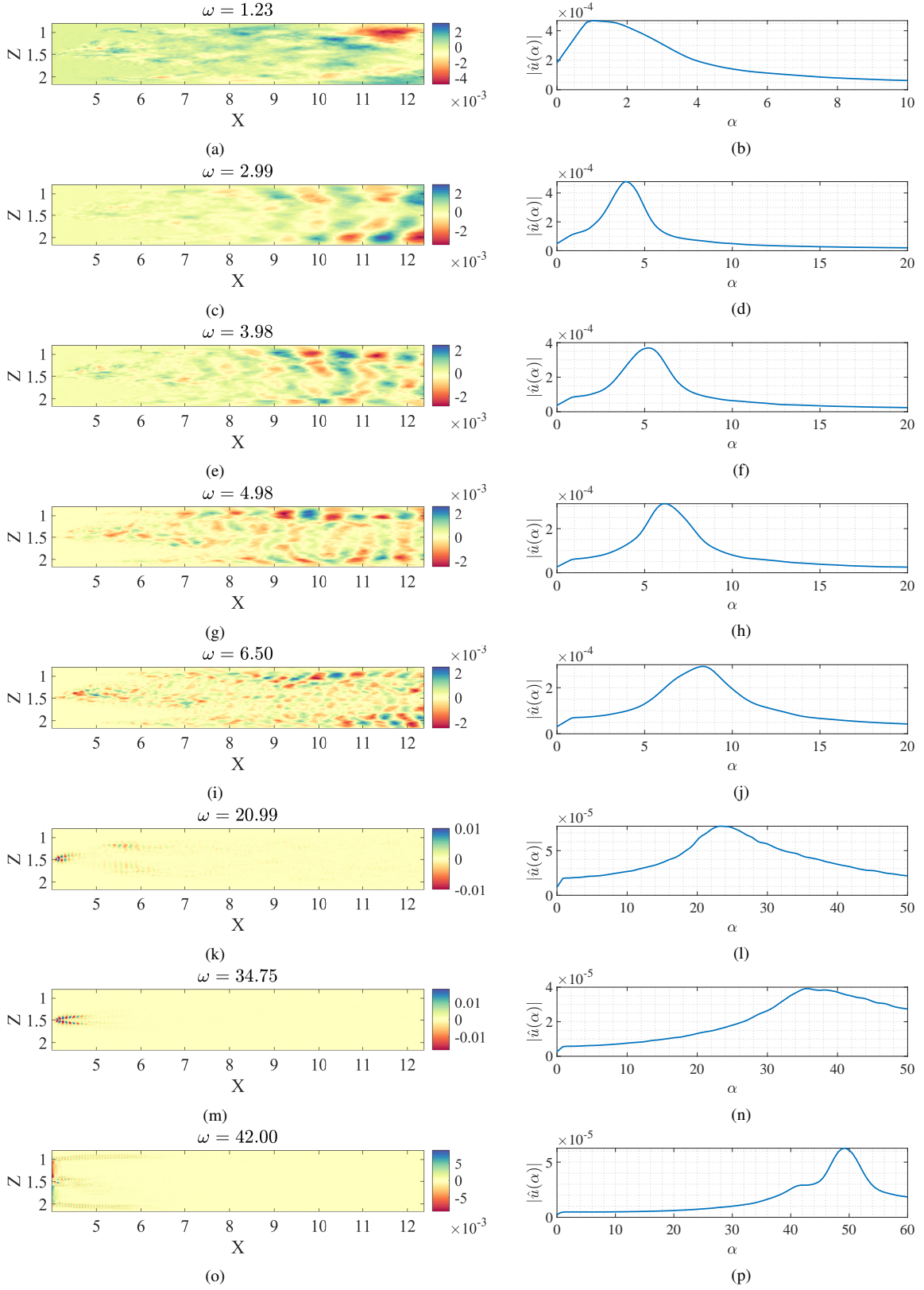


Figure 9: (Left) Axial component of the real part and (right) Fourier amplitudes in the streamwise direction of several leading DMD modes averaged in the wall-parallel planes  $y = 0$  ((a-j) and (o-p)),  $y = -0.41$  (k-l) and  $y = -0.65$  (m-n). The modes are ordered from top to bottom according to their frequency, those in subframes (a-h) and (o-p) being four of the five pairs selected with  $\gamma = 40000$ .

283 Decreasing the sparsity promoting parameter allows retrieving a more complete basis, inducing  
284 a negligible performance loss coefficient with respect to the POD, with a smaller set of modes  
285 (250 instead of 300). The additional DMD modes are mostly harmonics of the five pairs recov-  
286 ered for the highest value of  $\gamma$ , although some lower-amplitude modes, linked to the dynamics  
287 of the towers's wake are found as well. Unlike the largest-amplitude ones, these DMD modes  
288 are localized in the near wake, in the central region of the domain, corresponding to the tower's  
289 (and nacelle's) wake and are characterized by a much higher streamwise wavenumber. More-  
290 over, high-amplitude DMD modes localized in the far wake and characterized by a very low  
291 frequency, lying in the range of the wake meandering, are found as well.

## 292 6. OUTLOOK

293 These results show that the most dynamically relevant DMD modes are related to the tip  
294 vortices in the near wake and to larger-scale structures in the far wake, pulsating with low fre-  
295 quency reaching the range of the wake meandering. The main result of this analysis is that  
296 a consistent part of the dynamically relevant coherent structures in the wake is due to these  
297 large-scale modes.

298 Therefore, a very-low-dimensional reduced-order model (ROM) would mostly take into ac-  
299 count these low-frequency modes, but at the price of a large performance loss. Whereas, a  
300 low-dimensional model of the wake taking into account the harmonics or subharmonics of the  
301 largest-amplitude modes, together with other lower-amplitude modes linked to the tower's and  
302 nacelle's vortex shedding, will ensure a negligible performance loss, with a smaller number  
303 of modes than the POD. This is a very useful indication to develop accurate ROMs based on  
304 DMD in the future, which would eventually lead to the design of optimized wind farms layout  
305 and control to increase the energy density produced.

## 306 7. ACKNOWLEDGEMENTS

307 This paper is an extended version of our conference paper from 16th SDEWES Conference,  
308 Dubrovnik, Croatia, 10-15 October 2021.

## 309 References

- 310 [1] P. A. Østergaard, N. Duic, Y. Noorollahi, S. A. Kalogirou, Recent advances in renewable  
311 energy technology for the energy transition, *Renewable Energy* 179 (2021) 877–884.
- 312 [2] Liuwen, Yang, *Combustion instabilities in gas turbine engines: Operational experience,*  
313 *fundamental mechanisms, and modeling*, 1, 2006.
- 314 [3] D. Medici, *Experimental studies of wind turbine wakes: power optimisation and mean-*  
315 *dering*, Ph.D. thesis, KTH, 2005.
- 316 [4] P. A. Østergaard, N. Duic, Y. Noorollahi, H. Mikulcic, S. Kalogirou, Sustainable devel-  
317 opment using renewable energy technology, *Renewable Energy* 146 (2020) 2430–2437.
- 318 [5] P. A. Østergaard, N. Duic, Y. Noorollahi, S. Kalogirou, Latest progress in sustainable  
319 development using renewable energy technology, *Renewable Energy* 162 (2020) 1554–  
320 1562.

- 321 [6] I. R. E. Agency, Future of wind: Deployment, investment, technology, grid integration  
322 and socio-economic aspects (A Global Energy Transformation paper), Technical Report,  
323 IRENA, 2019.
- 324 [7] I. R. E. Agency, Renewable capacity statistics 2021, Technical Report, IRENA, 2021.
- 325 [8] I. E. Agency, Renewable 2020, Analysis and forecast to 2025, Technical Report, Fuel  
326 report November 2020, 2020.
- 327 [9] I. R. E. Agency, Renewable power generation costs in 2019, Technical Report, IRENA,  
328 2021.
- 329 [10] R. Wisler, J. Rand, J. Seel, P. Beiter, E. Baker, E. Lantz, P. Gilman, Expert elicitation  
330 survey predicts 37% to 49% declines in wind energy costs by 2050, *Nat. Energy* (2021).
- 331 [11] R. J. Stevens, C. Meneveau, Flow structure and turbulence in wind farms, *Annual review  
332 of fluid mechanics* 49 (2017).
- 333 [12] G. Berkooz, P. Holmes, J. L. Lumley, The proper orthogonal decomposition in the analysis  
334 of turbulent flows, *Annual review of fluid mechanics* 25 (1993) 539–575.
- 335 [13] N. Hamilton, M. Tutkun, R. B. Cal, Low-order representations of the canonical wind  
336 turbine array boundary layer via double proper orthogonal decomposition, *Physics of  
337 Fluids* 28 (2016) 025103. doi:10.1063/1.4940659.
- 338 [14] N. Ali, N. Hamilton, D. DeLucia, R. Bayoan Cal, Assessing spacing impact on coherent  
339 features in a wind turbine array boundary layer, *Wind Energy Science (Online)* 3 (2018).  
340 doi:10.5194/wes-3-43-2018.
- 341 [15] G. De Cillis, S. Cherubini, O. Semeraro, S. Leonardi, P. De Palma, Pod-based analysis of  
342 a wind turbine wake under the influence of tower and nacelle, *Wind Energy* 24 (2021).
- 343 [16] P. J. Schmid, Dynamic mode decomposition of numerical and experimental data, *Journal  
344 of fluid mechanics* 656 (2010) 5–28.
- 345 [17] M. Ilak, C. W. Rowley, Modeling of transitional channel flow using balanced proper  
346 orthogonal decomposition, *Phys. Fluids* 20 (2008) 034103.
- 347 [18] M. A. Bucci, S. Cherubini, J. C. Loiseau, J. C. Robinet, Influence of freestream turbulence  
348 on the flow over a wall roughness, *Physical Review Fluids* 6 (2021) 063903.
- 349 [19] R. Rajasegar, J. Choi, B. McGann, A. Oldani, T. Lee, S. D. Hammack, C. D. Carter,  
350 J. Yoo, Comprehensive combustion stability analysis using dynamic mode decomposition,  
351 *Energy & Fuels* 32 (2018) 9990–9996. doi:10.1021/acs.energyfuels.8b02433.
- 352 [20] M. Liu, L. Tan, S. Cao, Method of dynamic mode decomposition and reconstruction with  
353 application to a three-stage multiphase pump, *Energy* 208 (2020).
- 354 [21] M. Liu, L. Tan, S. Cao, Dynamic mode decomposition of gas-liquid flow in a rotodynamic  
355 multiphase pump, *Renewable Energy* 139 (2019) 1159–1175.

- 356 [22] Y. Han, L. Tan, Dynamic mode decomposition and reconstruction of tip leakage vortex  
357 in a mixed flow pump as turbine at pump mode, *Renewable Energy* 155 (2020) 725–734.
- 358 [23] G. V. Iungo, C. Santoni-Ortiz, M. Abkar, F. Porté-Agel, M. A. Rotea, S. Leonardi, Data-  
359 driven reduced order model for prediction of wind turbine wakes, in: *J. Phys. Conf. Ser.*,  
360 volume 625, IOP Publishing, 2015, p. 012009.
- 361 [24] S. Le Clainche, L. S. Lorente, J. M. Vega, Wind predictions upstream wind turbines from  
362 a lidar database, *Energies* 11 (2018) 543.
- 363 [25] M. Debnath, C. Santoni, S. Leonardi, G. V. Iungo, Towards reduced order modelling for  
364 predicting the dynamics of coherent vorticity structures within wind turbine wakes, *Philos-*  
365 *ophical Transactions of the Royal Society A: Mathematical, Physical and Engineering*  
366 *Sciences* 375 (2017).
- 367 [26] M. R. Jovanović, P. J. Schmid, J. W. Nichols, Sparsity-promoting dynamic mode decom-  
368 position, *Physics of Fluids* 26 (2014) 024103.
- 369 [27] S. Pope, S. Pope, P. Eccles, C. U. Press, *Turbulent Flows*, Cambridge University Press,  
370 2000.
- 371 [28] C. Santoni, U. Ciri, M. Rotea, S. Leonardi, Development of a high fidelity cfd code  
372 for wind farm control, in: *2015 American Control Conference (ACC)*, IEEE, 2015, pp.  
373 1715–1720.
- 374 [29] J. N. Sorensen, W. Z. Shen, Computation of wind turbine wakes using combined navier-  
375 stokes/actuator-line methodology, in: *1999 European Wind Energy Conference and Ex-*  
376 *hibition*, 1999, pp. 156–159.
- 377 [30] P. Orlandi, S. Leonardi, Dns of turbulent channel flows with two-and three-dimensional  
378 roughness, *Journal of Turbulence* (2006) N73.
- 379 [31] P. Orlandi, *Fluid flow phenomena: a numerical toolkit*, volume 55, Springer Science &  
380 Business Media, 2012.
- 381 [32] C. Santoni, K. Carrasquillo, I. Arenas-Navarro, S. Leonardi, Effect of tower and nacelle  
382 on the flow past a wind turbine, *Wind Energy* 20 (2017) 1927–1939.
- 383 [33] I. Orlandi, A simple boundary condition for unbounded hyperbolic flows, *Journal of*  
384 *Computational Physics* 21 (1976) 251–269.
- 385 [34] L. Sirovich, Turbulence and the dynamics of coherent structures. parts i-iii., *Quarterly of*  
386 *applied mathematics* 45 (1987) 561–590.
- 387 [35] J. Jeong, F. Hussain, On the identification of a vortex, *Journal of Fluid Mechanics* 285  
388 (1995) 69–94. doi:10.1017/S0022112095000462.
- 389 [36] K. K. Chen, J. H. Tu, C. W. Rowley, Variants of dynamic mode decomposition: boundary  
390 condition, koopman, and fourier analyses, *J. Nonlinear Sci.* 22 (2012) 887–915.

- 391 [37] X. Mao, J. Sørensen, Far-wake meandering induced by atmospheric eddies in flow past a  
392 wind turbine, *Journal of Fluid Mechanics* 846 (2018) 190–209.
- 393 [38] V. Gupta, M. Wan, Low-order modelling of wake meandering behind turbines, *Journal*  
394 *of Fluid Mechanics* 877 (2019) 534–560.
- 395 [39] F. Viola, G. V. Iungo, S. Camarri, F. Porté-Agel, F. Gallaire, Prediction of the hub vortex  
396 instability in a wind turbine wake: stability analysis with eddy-viscosity models calibrated  
397 on wind tunnel data, *Journal of Fluid Mechanics* 750 (2014).
- 398 [40] G. De Cillis, S. Cherubini, O. Semeraro, S. Leonardi, P. De Palma, Stability and optimal  
399 forcing analysis of a wind turbine wake: comparison with pod, *Renewable Energy* 181  
400 (2022) 765–785.